A Probabilistic Approach with Built-in Uncertainty Quantification for the Calibration of a Superelastic Constitutive Model from Full-field Strain Data

Harshad M. Paranjape[a,*], Kenneth I. Aycock[b], Craig Bonsignore[a], Jason D. Weaver[b], Brent A. Craven[b], Thomas W. Duerig[a]

[a] *Confluent Medical Technologies, Inc. 47533 Westinghouse Drive, Fremont, CA 94539, United States.*

[b] *U.S. Food and Drug Administration, Center for Devices and Radiological Health, Office of Science and Engineering Laboratories, Division of Applied Mechanics., Silver Spring, MD 20993, United States.*

Abstract

We implement an approach using Bayesian inference and machine learning to calibrate the material parameters of a constitutive model for the superelastic deformation of NiTi shape memory alloy. We use a diamond-shaped specimen geometry that is suited to calibrate both tensile and compressive material parameters from a single test. We adopt the Bayesian inference calibration scheme to take full-field surface strain measurements obtained using digital image correlation together with global load data as an input for calibration. The calibration is performed by comparing these two experimental quantities of interest with the corresponding results from a simulation library built with the superelastic forward finite element model. We present a machine learning based approach to enrich the simulation library using a surrogate model. This improves the calibration accuracy to the extent permitted by the accuracy of the underlying material model and also improves the computational efficiency. We demonstrate, verify, and partially validate the calibration results through various examples. We also demonstrate how the uncertainty in the calibrated superelastic material parameters can propagate to a subsequent simulation of fatigue loading. This approach is versatile and can be used to calibrate other models of superelastic deformation from data obtained using various modalities. This probabilistic calibration approach can become an integral part of a framework to assess and communicate the credibility of simulations performed in the design of superelastic NiTi articles such as medical devices. The knowledge obtained from this calibration approach is most effective when the limitations of the underlying model and the suitability of the training data used to calibrate the model are understood and communicated.

*Corresponding author

Email address: harshad.paranjape@confluentmedical.com (Harshad M. Paranjape)

Keywords: NiTi, Finite element modeling, Uncertainty Quantification, Digital Image Correlation, Bayesian Inference

1. Introduction

Simulation of the thermo-mechanical response of Nickel-Titanium (NiTi) shape memory alloys (SMAs) remains a topic of significant interest in the scientific community and in engineering practice. The reason for scientific interest in NiTi simulation is due to the challenges posed by the multi-scale microstructure, highly non-linear and inelastic constitutive response, anisotropy of the material properties, and the asymmetry in tension vs. compression response. The engineering interest in NiTi simulation is due to the extensive use of superelastic NiTi in the manufacturing of medical implants and devices and due to the strong potential of shape memory NiTi as an actuator material in the aeronautics industry. When computational methods are used to simulate NiTi response in these fields, a model is typically used to predict either global quantities of interest such as the radial force of a stent or the actuation load of a spring actuator, or to obtain local quantities of interest such as the local strain distribution in an implant under physiological boundary conditions. These quantities of interest are then leveraged for some specific context of use (e.g., as part of the performance or durability assessment).

As with the broader simulation community, a topic of emerging importance to NiTi simulation is the necessity to quantify and report the credibility of any computational modeling that is performed for a specific context of use [1]. Organizations in both medical device and aeronautics communities recognize that simulation will play an increasingly prominent role in decision making throughout the lifecycle of a particular product. They identify credibility assessment of the models and uncertainty quantification of the simulation results as a key component of the future development in the simulation practices. Morrison et al. note that sufficiently-credible computational modeling evidence can act as a support in the regulatory applications of medical devices [2]. NASA Vision 2040 report specifically incorporates uncertainty quantification as a key focus area [3].

The simulated response from any computational model is influenced by the material parameters used as constitutive model inputs. As a consequence, the credibility of simulation results is affected by the specific values and the uncertainty of the material parameters that are used. The material parameters for a particular computational model are generally calibrated by comparing experimental measurements (e.g., load or strain) with computational simulations of the experiment. While *ad hoc* or trial-and-error approaches are the most common, recently, various efforts have employed statistical or probabilistic methods such as Bayesian inference (BI) to solve the inverse problem of calibrating the material parameters [4]. The benefit of probabilistic methods over deterministic optimizations schemes for calibration (e.g., finite element model updating, gap method, virtual fields method) is that the probabilistic methods inherently

furnish uncertainty information about the fitted parameters, rather than simply providing the optimum parameters. Gogu et al. presented a BI approach for the determination of macroscopic elastic stiffness of truss-type metallic structure [5]. Liu and Au used BI to determine the material parameters of a phenomenological elasto-plastic model for the hysteretic load-displacement response of a composite material [6]. Castillo and Kalidindi reported a calibration method based on BI to determine the single crystal elastic constants of metallic materials using indentation load-displacement data [7]. Ricciardi et al. demonstrated the calibration of a crystal plasticity model using a BI approach [8]. Two efforts in the literature have specifically applied BI to the calibration of NiTi SMA constitutive model properties. Crews and Smith used BI to estimate the material parameters of a phenomenological model for actuation response of NiTi due to the shape memory effect [9]. Honarmandi et al. presented another example of calibration of a model for shape memory effect in NiTi [10]. These two examples addressed the calibration of models to simulate the thermally-induced response of NiTi and not the superelastic response. A common aspect to the examples cited above is that they used a single experimental comparator (e.g., global load data) to arrive at the calibrated material parameters.

Generally, there is a three-fold reason to perform calibration using a relatively large comparator data set. First, the uncertainty in the calibrated material properties reduces as the experimental sample size increases. Second, a larger sample size reduces the effect of any prior assumptions made related to the distribution of material parameters. In the context of BI, this phenomenon is sometimes referred to as the *data overwhelming the prior*. Third, a model calibration performed using a single comparator such as the global load may furnish material parameters that are optimized to give the correct load response. However, when the same model is used in another context of use (e.g., to simulate the local strains), then the predictions using the optimum parameters may significantly deviate from the expected response in terms of the quantity of interest. The first two concerns noted here can be simply addressed by performing a large number of experiments and using a larger number of observations to perform the calibration. However, the third concern can be alleviated by using a variety of comparators obtained using different experimental modalities to perform the calibration. One approach to obtain a large quantity of comparator data other than load is to use full-field surface strain measurements on the test samples and using the strain field in the calibration process [11]. Digital image correlation (DIC) is a versatile method to obtain full-field surface strain data during tensile testing of materials. Rethore presented a general strategy for identifying material parameters from full-field displacement data [12]. Bertin et al. presented an example of a DIC-based constitutive model calibration approach where they developed a method to determine crystal plasticity parameters from small-scale DIC measurements [13].

While it is appealing to use BI on large comparator sample sizes or with comparator data from multiple sources, there is a practical limitation. Material property calibration using BI is typically implemented using a sampling method such as Markov Chain Monte Carlo. A reliable distribution of the cali-

brated material parameters is obtained by performing this sampling thousands of times with varying material parameters and comparing the predictions of the forward simulation in each step with the appropriate comparator. Performing simulations on-line during the sampling process is quite impractical, particularly when the constitutive response is highly non-linear such as in the case of NiTi alloys. A more tractable solution to this problem is to create a library of simulations beforehand with the input parameters spanning a reasonable parameter space. Then, during each sampling step this library can be queried to obtain the simulation results for the closest available material parameters in the library. This approach may work well when a small library is adequate. However, if a large number of parameters need to be calibrated, then the size of the library needed can be quite large. Alternately, this problem can be addressed by developing a surrogate forward model that can efficiently furnish the simulation results for any input material parameters. Recently, a few efforts have used machine learning (ML) to develop a surrogate model to speed up material model calibration using BI. Wu et al. used neural networks to speed-up the calibration of a homogenized elasto-plastic model for composites [14]. Lu et al. used deep learning to determine elasto-plastic material properties using indentation comparator data [15]. However, they did not use BI to determine parameter calibration uncertainties.

In summary, BI is a useful approach to determine constitutive model parameters and associated uncertainties. It is desirable to use multi-modal experimental data such as full-field strain data together with load data as a comparator. ML can be used to accelerate the BI parameter determination through the generation of a regression model that acts as a surrogate to the original constitutive model. To our knowledge, there is not an effort in the literature consisting of these three components to calibrate inelastic models in general and particularly the computational models for superelastic NiTi. Thus, we address this gap by implementing a combined BI and ML approach to calibrate and optimize superelastic NiTi constitutive model parameters from load and full-field surface strain data. We demonstrate this calibration approach with the phenomenological superelastic constitutive law implemented in Abaqus finite element modeling (FEM) framework [16]. However, the framework presented here is general and can be applied to other models for superelasticity. In Section 2, we describe the methods used in this calibration framework. In Section 3, we first present a basic example of the BI calibration approach when the load-displacement data from a tension test of NiTi is used as a comparator. We then present a detailed example demonstrating all elements of the proposed approach. Finally, we provide an application of this calibration approach. We demonstrate how the uncertainty in the calibrated material parameters obtained using BI can be propagated to subsequent simulations performed using these material properties. In Section 4, we critically assess the advantages and limitations of our approach.

2. Calibration Framework

We will first describe the calibration procedure in general. Later, we will specialize the procedure to the specific phenomenological model for superelastic deformation of NiTi.

Consider a constitutive law of the form $\boldsymbol{\sigma}(\boldsymbol{\varepsilon}, \boldsymbol{m})$ where $\boldsymbol{\sigma}$ is the stress, $\boldsymbol{\varepsilon}$ is the strain, and $\boldsymbol{m}$ is a material parameter vector. Let $\boldsymbol{Q}(\boldsymbol{\sigma}, \boldsymbol{a})$ be a vector of *Quantities of Interest* (QoI) that can be determined for a specific deformation geometry and boundary conditions. Here $\boldsymbol{a}$ is a parameter vector encoding the details such as geometry and boundary conditions that are necessary to calculate $\boldsymbol{Q}$. For example, $\boldsymbol{Q}$ could be the global load measured during the deformation of a specimen at a fixed imposed displacement. Or $\boldsymbol{Q}$ could be the strain tensor at a specific location in the specimen at an imposed deformation. Since $\boldsymbol{Q}$ is based on the constitutive law, it indirectly depends on $\boldsymbol{m}$. The QoI can either be measured experimentally ($\boldsymbol{Q}^{\text{expt}}$) or computationally predicted ($\boldsymbol{Q}^{\text{sim}}$) using a model or numerical implementation of the constitutive law $\boldsymbol{\sigma}(\boldsymbol{\varepsilon}, \boldsymbol{m})$.

The simplest procedure to calibrate a model of $\boldsymbol{\sigma}(\boldsymbol{\varepsilon}, \boldsymbol{m})$ (i.e., to determine parameters $\boldsymbol{m}^{\text{cal}}$) is to minimize the difference between $\boldsymbol{Q}^{\text{expt}}$ and $\boldsymbol{Q}^{\text{sim}}$ while varying $\boldsymbol{m}$. A typical method to solve this inverse problem is to perform the minimization:

$$\boldsymbol{m}^{\text{cal}}_{\text{LSQ}} := \arg\min_{\boldsymbol{m}} \sum_{i}^{N} w_i \left(\boldsymbol{Q}^{\text{sim}}_{\boldsymbol{i}} - \boldsymbol{Q}^{\text{expt}}_{\boldsymbol{i}}\right)^2 . \tag{1}$$

Here N is the total number of observations of $\boldsymbol{Q}$ and w_i is the weight assigned to each observation. The objective function on the right hand side has a quadratic form and thus, we refer to this procedure as *least-squares calibration*. While this procedure is straight-forward, it does not furnish any information about the uncertainty of the calibration. BI on the other hand, provides a tool to determine $\boldsymbol{m}^{\text{cal}}$ and quantify the uncertainty in the calibration.

The general scheme of our calibration method is shown in Figure 1. In the first step of this calibration procedure, we standardize a test specimen geometry and a test protocol. Based on these, we can experimentally obtain a number of $\boldsymbol{Q}^{\text{expt}}$ values. In parallel, we setup a simulation with the constitutive law $\boldsymbol{\sigma}(\boldsymbol{\varepsilon}, \boldsymbol{m})$, the virtual specimen geometry, and boundary conditions based on the test protocol. The simulation acts as a forward model and furnishes a number of $\boldsymbol{Q}^{\text{sim}}$ values. In the simulation, we vary the values of the material parameters $\boldsymbol{m}$ to span the typical material parameter space and obtain the corresponding $\boldsymbol{Q}^{\text{sim}}$ values. Thus, we build a simulation library that maps $\boldsymbol{m}$ to $\boldsymbol{Q}^{\text{sim}}$. In the next step, we use BI to obtain $\boldsymbol{m}^{\text{cal}}$ and their uncertainty. We first describe the BI component of this procedure below.

2.1. Bayesian Inference for Calibration and Uncertainty Quantification

The probability distribution of the material parameters given a set of experimentally measured quantities of interest ($P(\boldsymbol{m}|\boldsymbol{Q}^{\text{expt}})$ or posterior) can be expressed in terms of the probability distribution of the material parameters

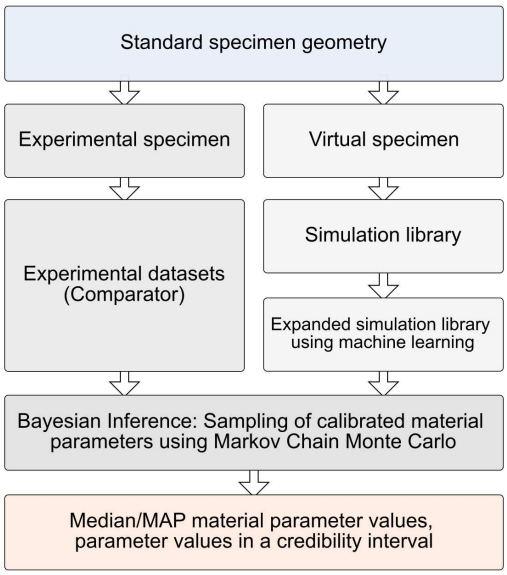


Figure 1: A summary of the Bayesian Inference material parameter calibration method. A flowchart listing the key components of the method is shown.

based on prior knowledge ($P(\boldsymbol{m})$ or prior) and the probability of observing an experimental response $\boldsymbol{Q}^{\text{expt}}$ if the material parameters were actually $\boldsymbol{m}$ ($P(\boldsymbol{Q}^{\text{expt}}|\boldsymbol{m})$ or likelihood) using the Bayes' theorem

$$P(\boldsymbol{m}|\boldsymbol{Q}^{\text{expt}}) = \frac{P(\boldsymbol{m})P(\boldsymbol{Q}^{\text{expt}}|\boldsymbol{m})}{P(\boldsymbol{Q}^{\text{expt}})}. \tag{2}$$

The denominator, $P(\boldsymbol{Q}^{\text{expt}})$, is a normalization constant and referred to as the probability of the evidence [17]. In BI, this factor is typically not calculated and simply $P(\boldsymbol{m}|\boldsymbol{Q}^{\text{expt}}) \propto P(\boldsymbol{m})P(\boldsymbol{Q}^{\text{expt}}|\boldsymbol{m})$.

Bayes' theorem in the form described above furnishes a probability distribution of the material parameters given certain experimental data. The optimum or fitted parameters can be reported from this distribution in terms of one of the point estimates. Some common point estimates are mean, median, or maximum a posteriori (MAP). The uncertainty in the fitted parameters can be reported in terms of the *credible intervals* of the distribution. Credible intervals are the probabilistic statistics counterpart to the confidence intervals in the frequentist statistics. Thus, uncertainty estimation of calibration is built into this method. The prior $P(\boldsymbol{m})$ incorporates an expert's knowledge about the parameter space for a particular constitutive law. For example, the Young's modulus of most metals is in the GPa range with a larger probability between 10 to 100 GPa. The likelihood ($P(\boldsymbol{Q}^{\text{expt}}|\boldsymbol{m})$) of observing a particular experimental response for a given material parameters can be calculated using a forward model that furnishes $\boldsymbol{Q}$ as a function of $\boldsymbol{m}$. A simulation library that maps $\boldsymbol{m}$ to $\boldsymbol{Q}^{\text{sim}}$

across the parameter space can be used to calculate the likelihood. Thus,

$$P(\boldsymbol{Q}^{\text{expt}}|\boldsymbol{m}) := c \cdot \prod_{i}^{N} \exp\left(-w_i \frac{(\boldsymbol{Q_i}^{\text{sim}} - \boldsymbol{Q_i}^{\text{expt}})^2}{2s^2}\right), \tag{3}$$

where c is a constant, w are the weights assigned to the observations, and s^2 is the standard deviation of the lumped error in the experimental measurements [4]. The exponent in this expression is a loss function that quantifies the discrepancy between the experimental measurement and a *true* response observed for a particular $\boldsymbol{m}$ and reaches a maximum value when the discrepancy between the observed and the true response is minimum [18]. If multiple independent experimental observations are available and the errors in the observations (s^2) are assumed to be constant, the total likelihood can be modeled as a multivariate Gaussian distribution, resulting in the product term in Equation (3).

In most practical situations, no analytical expression for any of the terms on the right hand side of Equation (2) is available. Hence, a numerical sampling procedure is generally used to indirectly obtain the posterior distribution of the material properties from the prior distribution and the likelihood function. In this calibration scheme, we use a Metropolis-Hastings variant of the Markov Chain Monte Carlo (MCMC) sampler to obtain the fitted parameter distribution. An MCMC sampler operates in three steps [4, 17, 19]. First, the material parameters are initiated at a certain point in the parameter space ($\boldsymbol{m_o}$) and the posterior probability at that point is calculated knowing the likelihood function and the prior distribution. Second, a new point $\boldsymbol{m}_i$ is drawn in the material parameter space and the posterior probability at the new point is calculated. In the third step, the new sample is accepted if the new probability is larger than the previous. However, the new sample is also accepted if the acceptance probability is larger than a random number drawn from the uniform standard distribution. Steps two and three are repeated until a certain number of samples are obtained. From this sampled posterior distribution, the point estimates and the credibility interval described above can be readily calculated to obtain the optimum material parameters and their uncertainty.

There is one challenge in executing the approach described so far. One of the terms in the likelihood function in Equation (3) is $\boldsymbol{Q}^{\text{sim}}$. If the forward model used to calculate $\boldsymbol{Q}^{\text{sim}}$ from a sampled $\boldsymbol{m}$ is fairly complex, then it may be challenging to use the model online during the MCMC sampling. Online calculation of $\boldsymbol{Q}^{\text{sim}}$ may be avoided by building a library of $\boldsymbol{Q}^{\text{sim}}$ beforehand and then querying the library during the sampling process for the closest available material parameters to $\boldsymbol{m}_i$. This is akin to doing a nearest-neighbor interpolation on the simulation results in the parameter space. A superior approach is to develop a computationally efficient surrogate model that is derived from the available simulation results to furnish $\boldsymbol{Q}^{\text{sim}}$ for any $\boldsymbol{m}$. We describe the development of such a surrogate forward model below.

2.2. Surrogate Model from the Simulation Library using Machine Learning

A surrogate model that can furnish $\boldsymbol{Q}^{\text{sim}}$ for any $\boldsymbol{m}$ can be built using any regression scheme if a library of previously run simulations that map $\boldsymbol{m} \rightarrow \boldsymbol{Q}^{\text{sim}}$ is available. In this work, we choose a ML regression method – kernel support vector machine (SVM) – to build the surrogate model [20]. One regression model is trained for each QoI that will be used for material parameter calibration. Once a regression model is trained, it can be used in the MCMC sampler described above to obtain the likelihood $P(\boldsymbol{Q}^{\text{expt}}|\boldsymbol{m})$ for $\boldsymbol{m}$ that is not present in the simulation library.

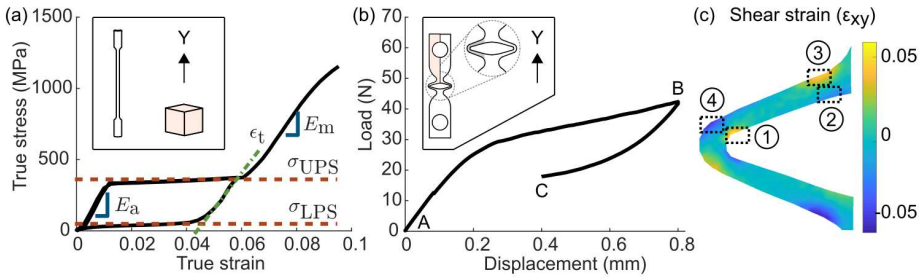


Figure 2: Test specimens and the quantities of interest (QoIs). (a) Stress-strain curve of a NiTi dogbone specimen tested per ASTM 2516. The specimen geometry is shown on the left inside the inset. The single element simulation geometry used to model the tensile response of this specimen is shown on the right inside the inset. (b) A diamond NiTi specimen load-displacement response during an isothermal tensile test. The specimen geometry is shown inside the inset. The simulation geometry consists of a quarter diamond and is highlighted in orange in the inset. (c) A typical surface strain field in a NiTi diamond specimen obtained using a digital image correlation (DIC) measurement during a tensile test. In all cases, the loading direction is along Y.

2.3. BI and ML Calibration Approach for a Superelastic Material Model

Now we specialize the BI- and ML-based calibration approach to a phenomenological model for superelastic deformation behavior. Figure 2(a) shows the constitutive response of a typical superelastic NiTi specimen at room temperature. The model of Auricchio and Taylor is widely used to simulate such deformation response [16, 21]. The model is developed in an infinitesimal strain framework. Stress and temperature are considered as the independent variables. The inherent deformation mechanism of austenite to martensite phase transformation is simulated. The total martensite phase fraction at a material point is taken as the internal variable. The total strain at a material point is additively decomposed into an elastic and a transformation component ($\varepsilon = \varepsilon_{\text{e}} + \varepsilon_{\text{tr}}$). The elastic behavior of the austenite and martensite phase is assumed to be isotropic. The evolution of the internal variable is determined using a rate-independent formulation. This model is implemented in various commercial FEM packages including Abaqus (Simulia Dassault Systemes, version 2019). The model accepts six key material inputs: Young's modulus of austenite (E_{A}), Young's modulus of martensite (E_{M}), maximum transformation strain (ε_{t}), upper plateau stress

in tension (σ_{UPS}), lower plateau stress in tension (σ_{LPS}), and the compression plateau stress (σ_{CPS}). The connection of these six parameters to the superelastic constitutive response is schematically shown in Figure 2(a). While σ_{CPS} is dependent on the microstructure and the processing history of a specific NiTi specimen, often σ_{CPS} is not calibrated in simulations and it is assumed that the ratio $\sigma_{\mathrm{CPS}}/\sigma_{\mathrm{UPS}}$ approximately equals 1.5 [22, 23]. We do not make this assumption. The model allows to specify the hardening of upper and lower plateaus. We assume a fixed hardening of 30 MPa. The Abaqus implementation of the model takes other minor inputs. Those are not addressed in this work. Plasticity is also not addressed. In summary, the goal of this BI- and ML-based calibration approach is to solve the inverse problem of determining $\boldsymbol{m} = \{E_{\mathrm{A}}, E_{\mathrm{M}}, \varepsilon_{\mathrm{t}}, \sigma_{\mathrm{UPS}}, \sigma_{\mathrm{LPS}}, \sigma_{\mathrm{CPS}}\}$ given a set of experimental inputs.

2.3.1. Calibration Using Global Stress Data

As a first example of the BI-based calibration approach described in Section 2.1, we calibrate the superelastic material model using the observations from a tensile test on a dogbone specimen that was laser-cut from NiTi tubing. We heat treated a commercial tubing material with 50.8at.%Ni composition such that it was superelastic at room temperature. The dogbone test specimen geometry is shown in Figure 2(a) inset. An experimental stress-strain curve obtained at room temperature according to the standard test method in ASTM F2516 [24] is shown in Figure 2(a). The test method consists of loading the specimen in displacement control to an engineering strain of 6%, unloading to zero load, and finally loading to fracture. We performed the test on an Instron 5969 load frame at a nominal strain rate of $1.4 \times 10^{-4}\,\mathrm{s}^{-1}$. The axial strain in the gage was measured using the built-in video extensometer in the Instron load frame. We calculated the axial stress in the specimen gage from the load measured by a 1 kN load cell on the Instron load frame and the cross-section dimensions of the test specimen measured prior to test. We extracted axial true stress at 82 points along the stress-strain curve such that the points were equally separated in time. These axial stress values will serve as $\boldsymbol{Q}^{\mathrm{expt}}$ in the material parameter calibration.

We created a single element Abaqus/Standard FEM simulation of the loading condition used in the experiment. The deformation in the gage of a dogbone-type NiTi specimen can be adequately captured by a single element model. We modeled the response of the single element model using the superelastic material model in Abaqus. We created a library of 1843 instances of the simulation with the material parameters in each case selected using Latin hypercube sampling of the following parameter space: $E_{\mathrm{A}} \in [10\,\mathrm{GPa}, 80\,\mathrm{GPa}]$, $E_{\mathrm{M}} \in [10\,\mathrm{GPa}, 50\,\mathrm{GPa}]$, $\varepsilon_{\mathrm{t}} \in [0.03, 0.07]$, $\sigma_{\mathrm{UPS}} \in [100\,\mathrm{MPa}, 600\,\mathrm{MPa}]$, $\sigma_{\mathrm{LPS}} \in [10\,\mathrm{MPa}, 400\,\mathrm{MPa}]$, and $\sigma_{\mathrm{CPS}} \in [150\,\mathrm{MPa}, 700\,\mathrm{MPa}]$. We started with smaller library sizes and eventually settled with 1843 simulations since they furnished reasonable results for this example. Unphysical material parameter combinations such as $\sigma_{\mathrm{UPS}} \leq \sigma_{\mathrm{LPS}}$ were not instantiated. We applied boundary conditions that were equivalent to the experimental boundary conditions used in the dogbone tensile test described above. From the result of each simulation, we extracted axial true stress

at 82 frames that were equally separated in time. We selected the time points such that the simulation axial stress data was available at the same time instants at which the axial stress from the experiment was extracted. This is rather straightforward to do considering that both the experiment and simulation were executed in displacement control with a constant strain rate boundary condition. These axial stress values will serve as $\boldsymbol{Q}^{\text{sim}}$ in the material parameter calibration.

From the experimental stress-strain data for the dogbone and the simulation results in the library, we performed material property calibration. All data analysis was performed in Matlab (The Mathworks, Inc., version R2018a). We selected global axial true stress at 82 locations along the stress-strain curve as the QoI for this BI calibration example. From these QoI, we first performed a traditional weighted least-squares calibration to obtain the optimum values of the six material parameters. For this, we performed minimization as specified in Equation (1) using a weight at each point that was proportional to the local slope of the experimental stress-strain curve. The specific weights used at 82 QoIs are listed in Supplementary Data. Weights proportional to the local slope of the stress-strain curve appear to equalize the influence of data points from the plateaus vs. the points from the elastic regimes. Note that such minimization provides the optimum parameters among the parameter combinations in the 1843 simulation instances. Then, we performed a BI calibration using a Goodman and Weare affine invariant ensemble MCMC sampler [25]. We used 100 walkers and drew 4×10^6 samples. We used an uninformative flat prior. That is, each of the six material parameters had a uniform probability distribution in the parameter space described in the paragraph above. In BI, the choice of prior can influence the results. We performed a limited study and found out that the results in this case are relatively insensitive to the choice of prior distribution. The details of prior effect are provided in Supplementary Data. We initialized the walkers with material parameters drawn from a normal distribution centered at the mean of the parameter space and with a standard deviation equal to 1/10th of the parameter space span. We defined the likelihood function as described in Equation (3). We discarded the first 50% of the samples from the posterior as the burn-in period. From the marginal posterior distribution for each material parameter, we calculated MAP, median, and 95% credible intervals. For this example, we did not perform simulation library enrichment using the ML approach described in Section 2.2 since we felt the library size of 1843 adequate to demonstrate the BI calibration approach.

For reference, the superelastic model parameters for this NiTi tubing material, determined using a semi-supervised trial-and-error approach, are - $\boldsymbol{m} =$ {31 GPa, 26 GPa, 0.045, 340 MPa, 70 MPa, 510 MPa}.

2.3.2. Calibration Using Global Load and Full-field Strain Data

As a second example of the BI- and ML-based approach, we calibrate the superelastic material model from global load and local strain observations obtained during a tensile test of a NiTi diamond specimen laser cut from a strip material with a composition of 50.8at.%Ni. The specimen geometry is shown

as an inset in Figure 2(b). We heat treated the NiTi strip material such that it was superelastic at room temperature. While the NiTi material used in this example has an identical composition as the tubing material in the previous example, the two materials have undergone different processing steps. Thus, the mechanical properties of this material in strip form can be different than those of the NiTi material in tubing form described in the previous section. Prior to the test, we applied a speckle pattern of finely ground charcoal on a matte white background to one surface of the diamond [26]. The experimental global load-displacement curve for this specimen is shown in Figure 2(b). We performed the test on an Instron 5969 load frame in displacement control at a nominal displacement rate of $2.94 \times 10^{-3}\,\mathrm{mm\,s^{-1}}$ at room temperature. During the tension test, we acquired photographs of the specimen gage (i.e., the curved struts on one side of the diamond) at a regular interval of 1 s using a Mitakon Zhongyi 20 mm f/2 4.5X Super Macro lens mounted on a Sony A7III digital mirrorless camera with 0.2 s exposure and ISO 400. We analyzed the photographs using Ncorr DIC software [27] implemented in Matlab to obtain the full-field 2D surface strain tensor. We used a subset radius of 30 pixels, subset spacing of 2 pixels, and strain window radius of 15 pixels in Ncorr. A sample full-field strain map (shear strain component) obtained using this DIC measurement is shown in Figure 2(c). We simultaneously recorded the global load-displacement data during the tensile test using the load cell and the crosshead movement respectively on the Instron load frame.

Based on the diamond specimen geometry and the experimental test boundary conditions described above, we created a simulation of the test. The diamond geometry has four-fold symmetry and thus, a quarter diamond as shown in Figure 2(b) inset was modeled to obtain the full deformation response. We modeled the response using the superelastic material model in Abaqus. We created a library of 544 instances of the simulation with the material parameters in each case selected using Latin hypercube sampling of the following parameter space: $E_\mathrm{A} \in [40\,\mathrm{GPa}, 80\,\mathrm{GPa}]$, $E_\mathrm{M} \in [20\,\mathrm{GPa}, 50\,\mathrm{GPa}]$, $\varepsilon_\mathrm{t} \in [0.035, 0.055]$, $\sigma_\mathrm{UPS} \in [300\,\mathrm{MPa}, 500\,\mathrm{MPa}]$, $\sigma_\mathrm{LPS} \in [100\,\mathrm{MPa}, 300\,\mathrm{MPa}]$, and $\sigma_\mathrm{CPS} \in [350\,\mathrm{MPa}, 700\,\mathrm{MPa}]$. Similar to the first example, the library size was determined by trial and error and unphysical material parameter combinations were not instantiated.

The QoI for the calibration scheme are the global load at 11 equally separated points between A and B in Figure 2(b), the global load at 11 equally separated points between B and C in Figure 2(b), and the local mean Green-Lagrange shear strain (ε_{xy}) at four regions in the specimen gage marked by ① to ④ in Figure 2(c) at the same 22 points during the loading cycle where the global load data was extracted. The rationale behind using the shear strain for calibration is provided in the Discussion section. Thus, 22 global load values and 88 local shear strain values were used as QoI for a total of 110 quantities. We extracted the $\boldsymbol{Q}^\mathrm{expt}$ from the load-displacement and DIC data obtained in the tensile test. The same quantities from each simulation in the simulation library were extracted using Python post-processing scripts.

From $\boldsymbol{Q}^\mathrm{expt}$ and $\boldsymbol{Q}^\mathrm{sim}$ from each of the simulation in the simulation library, we obtained the least-squares calibrated material parameter vector by perform-

ing the minimization in Equation (1). We used a weight of 0.25 for the strain QoI and a weight of 1 for load QoI. These weights and the fact that there are four times as many strain quantities as load ensure that the influence of local strain and global load on the calibration is equal. Subsequently, we performed a BI calibration using the same MCMC sampler as above. During MCMC sampling, we selected the simulation result with the nearest available $\boldsymbol{m}$ to the $\boldsymbol{m_i}$ in the MCMC draw to calculate the likelihood function value per the expression in Equation (3). We did this because $\boldsymbol{Q}^{\text{sim}}$ values are only available for those $\boldsymbol{m}$ vectors present in the simulation library and not for arbitrary $\boldsymbol{m}$. The nature of the prior and the initial walker values are similar to the example above. We generated 1×10^6 samples and rejected the first 20% of the samples as the burn-in samples. From the sampled posterior distribution of $\boldsymbol{m}$, we calculated median and MAP material parameters as well as the credible interval. We refer to these results as the results from *BI approach*.

To enrich the simulation library, we trained a regression SVM model to each of the 110 QoI using the results of all 544 simulation instances. Thus, a fitted SVM surrogate model furnishes the value of that QoI for an arbitrary $\boldsymbol{m}$ given as an input. We used the `fitrsvm` function in Matlab for this purpose. We used a Gaussian kernel with automatic scaling. We standardized the $\boldsymbol{m}$ during fitting since various material parameters are of widely different magnitudes. We used the automatic optimization option in the fitting function. This option internally finds such hyperparameters of the SVM that minimize the five-fold cross-validation loss and improve accuracy of the regression. The details of verification performed on the trained models are described in Supplementary Data. The verification study demonstrates that 544 simulation samples are adequate to furnish a reasonably accurate surrogate model in the six-dimensional parameter space.

Using the trained SVM surrogate models, we performed another calibration using BI. During the MCMC sampling for this calibration, the likelihood function in Equation (3) was calculated using the QoI values obtained from the trained models. A trained model can furnish $\boldsymbol{Q}^{\text{sim}}$ for an arbitrary $\boldsymbol{m}$. From the results of this calibration, we again computed descriptors such as median and MAP. We refer to these results as the results from *BI + ML approach*. In summary, we calculated three calibration results for this example: least-squares, BI approach, and BI + ML approach.

One motivation behind using the local strains as a QoI was the belief that they will furnish such calibrated material parameters that result in a more accurate simulation of the local strains. To determine if that is the case, we also performed a BI + ML calibration where the weights of the strain QoI were set to zero when calculating the likelihood function. Thus, only load QoI were used in this calibration. From the sampled marginal posterior probability distributions in this example, we calculated the median calibrated material properties.

To assess the robustness of the calibration, we performed a simple validation test. For the validation, we laser-cut a dogbone shaped specimen from the same NiTi strip material as that used to make the diamond described above. This dogbone specimen is different from the dogbone specimen laser cut from NiTi

tubing in the previous example. We performed a tensile test on the dogbone at room temperature. We created a simulation representative of this test and instantiated the simulation with median, MAP, and 95% credible interval parameters described above. We compared the simulation results with the tensile test measurements for the purpose of validation. A robust validation is typically performed on a model of equal or higher complexity compared to the model from which calibration results are obtained. Such study is not within the scope of this demonstration.

For reference, the superelastic model parameters for this NiTi strip material, determined using a semi-supervised trial-and-error approach, are - $\boldsymbol{m} = \{20$ GPa, 15 GPa, 0.04, 330 MPa, 180 MPa, 495 MPa$\}$.

3. Results

3.1. Calibration Using Global Stress Data

The results of least-squares and BI calibration for the example when the global stress was used as the QoI are listed in Table 1 and graphically shown in Figure 3. The results of least-squares calibration in the table reveal material parameter values in the general regime that is expected for a typical superelastic NiTi tubing material. However, $E_{\mathrm{A}} < E_{\mathrm{M}}$. This is unusual but not completely unexpected. Heat treated NiTi typically exhibits an intermediate R-phase formation during the austenite to martensite phase transformation. The intermediate phase transformation has a small transformation strain associated with it and it generally manifests as a softer austenite modulus in the constitutive response [28]. The marginal posterior probability distribution plots from BI calibration are shown in Figure 3(a). A narrow posterior probability distribution reflects a lower uncertainty in the calibration of that parameter. Thus, E_{M} and ε_{t} are calibrated with a lower uncertainty compared to the other four parameters. The lower uncertainty of these two calibrated parameters is also reflected in tighter bounds on the 95% credible interval listed in Table 1.

The calibration results are graphically shown in Figure 3(b). Overall, the MAP point estimate of the posterior distribution shows a closer match with the experimental data as emphasized in the inset. The closeness of the match can be quantified and reported in terms of the mean absolute percent error (MAPE) defined as,

$$\mathrm{MAPE} = \frac{1}{N}\sum_{i}^{N}\left|\frac{\boldsymbol{Q_i^{\mathrm{sim}}} - \boldsymbol{Q_i^{\mathrm{expt}}}}{\boldsymbol{Q_i^{\mathrm{expt}}}}\right|. \tag{4}$$

Here N is the total number of QoIs, which is 82 in this example. In the calculation of all MAPE values in this work, we did not consider the QoIs corresponding to the first two steps of the loading sequence in each experiment. This is because the load and the strains are close to zero in the first two steps of a tensile test and the errors at those steps are of lower concern. MAPE is tabulated in Table 1 and the smallest value is obtained for the MAP point estimate from BI calibration. This suggests that the MAP estimate furnished the most accurate parameter calibration. Overall the envelope of stress-strain response from

the 95% credible interval is broad. The calibrated and the experimental stress-strain curves diverge in the large strain regime. This is because plasticity is not incorporated in the simulations.

Fit description	E_a (GPa)	E_m (GPa)	ε_t	σ_{UPS} (MPa)	σ_{LPS} (MPa)	σ_{CPS} (MPa)	MAPE (%)
Least squares fit	26.2	32.7	0.0517	355	61.9	448	15.2
Bi fit (median)	25.0	33.0	0.0519	278	62.6	504	21.6
BI fit (MAP)	28.0	32.6	0.0513	342	55.4	482	12.9
BI fit (95% credible	11.6	25.8	0.0440	111	13.0	416	
interval)	33.6	38.1	0.0595	387	124	665	

Table 1: Results of calibration with global stress as the quantity of interest. MAPE refers to mean absolute percent error.

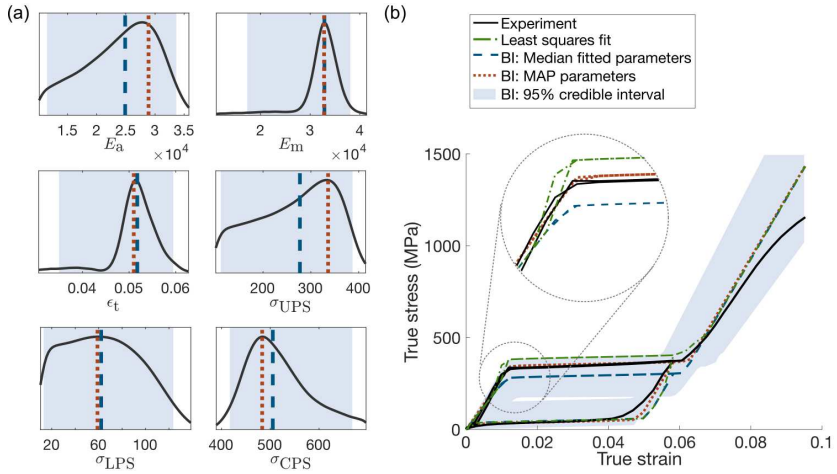


Figure 3: Results of calibration with global stress as the quantity of interest. (a) Posterior probability distribution of the six NiTi material model parameters sampled using the Markov-chain Monte Carlo scheme from a comparison of dogbone tensile test and simulations. (b) A qualitative comparison of the calibration on the same dogbone geometry.

3.2. Calibration Using Global Load and Full-field Strain Data

The results of calibration for the second example where global load and the full-field surface strain from DIC were used as the QoI are listed in Table 2. As previously noted, *BI fit* refers to the calibration that was performed with the library of simulations only and *BI + ML fit* refers to the calibration where ML regression model was used to enrich the simulation library. The results for BI fit are graphically shown in Figure 4. Overall, the elastic modulii are calibrated with a higher confidence compared to the other four parameters. This is evident from the relatively narrow shape of the marginal posterior probability

distribution for E_{A} and E_{M} in Figure 4(a). The least-squares calibrated parameters furnish results that provide the closest match with the experimental data. The second closest match is furnished by the MAP parameters from the BI fit. This is evident in the MAPE values in the table and in the load-displacement curves in Figure 4(b). The local shear strain (ε_{xy}) prediction with the median fitted parameters is compared with the DIC results at peak load in Figure 4(c). The qualitative comparison appears good. However, quantitatively the strains match only modestly. For example, if MAPE were calculated only for the load quantities of interest, then it is 11% for the median fitted parameters. This means that a larger error (MAPE) is contributed by strains than load. We discuss this aspect further in the Discussion section below.

The results for BI + ML fit are graphically shown in Figure 5. Both median and MAP estimates from the BI + ML approach provided a better fit than the BI approach and a marginally better fit than the least-squares approach. This is evident from the smaller MAPE in Table 2, narrower marginal posterior probability distributions for the fitted parameters in Figure 5(a) compared to the BI fit, and a relatively close match between the simulated load-displacement curves for the fitted parameter and the experimental data in Figure 5(b). The local shear strain prediction with the median fitted parameters is compared with the DIC results at peak load in Figure 5(c). The qualitative comparison appears good.

Fit description	E_{a} (GPa)	E_{m} (GPa)	ε_{t}	σ_{UPS} (MPa)	σ_{LPS} (MPa)	σ_{CPS} (MPa)	MAPE (%)
Least squares fit	49.4	39.2	0.0374	341	204	434	17.9
Bi fit (median)	56.1	35.7	0.0453	402	194	523	20.5
BI fit (MAP)	55.9	35.6	0.0524	470	108	475	22.2
BI fit (95% credible	40.3	21.9	0.0355	305	105	359	
interval)	75.9	41.4	0.0545	495	294	692	
BI + ML fit (median)	54.0	42.7	0.0377	355	204	407	17.3
BI + ML fit (MAP)	54.4	44.9	0.0368	351	201	408	17.4
BI + ML fit (95%	43.1	31.4	0.0351	328	191	379	
credible interval)	66.3	49.5	0.0442	387	218	437	

Table 2: Results of calibration for the diamond specimen using load and full-field strain data.

The use of both strain and load QoI in this example, rather than using just the macro load as the QoI, resulted in the calibrated material parameters that furnished a more accurate simulation of the local strains. We performed a BI + ML calibration using only the load QoI. This resulted in median $\boldsymbol{m}^{\mathrm{cal}} = \{48.9\text{ GPa}, 31.2\text{ GPa}, 0.0447, 342\text{ MPa}, 194\text{ MPa}, 494\text{ MPa}\}$. These values are different than the results listed in Table 2 for the median $\boldsymbol{m}^{\mathrm{cal}}$. These material parameters resulted in a MAPE of 21.9%, which is larger than the MAPE from median BI + ML parameters listed in the table (17.3%). The MAPE calculated for load values only was 3.71%, which is smaller than the MAPE for load from median BI + ML parameters listed in the table (5.3%). This means that the use of only load QoI resulted in a more accurate simulation of the load response,

but a less accurate simulation of the local strain response.

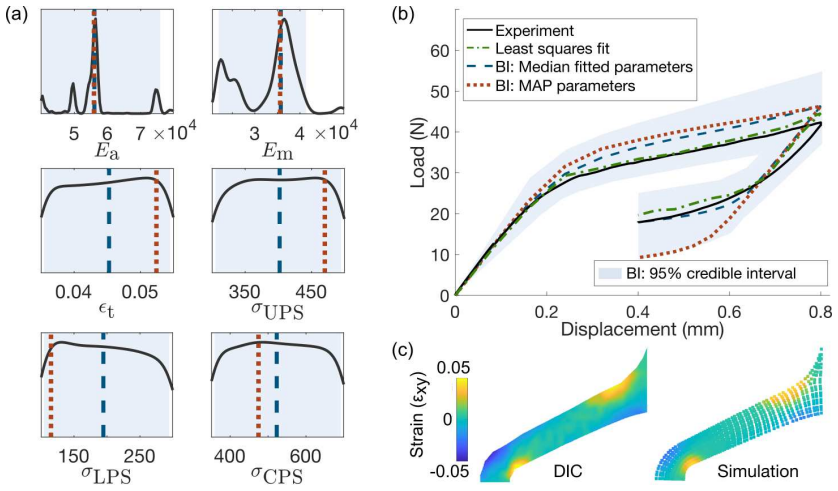


Figure 4: Results of BI calibration with global load and surface strains as the quantity of interest. (a) Marginal posterior probability distributions of the six NiTi material model parameters sampled using the Markov-chain Monte Carlo scheme from a comparison of diamond tensile test, DIC strain field data, and simulations. (b) A qualitative comparison of the calibration on the same diamond geometry. Load-displacement data from the tensile test is shown. (c) Comparison of the local shear strain at peak displacement during the tensile test as measured using DIC and from a simulation with the median fitted material properties.

The results of a simple validation test performed on a planar dogbone specimen using the material parameters obtained from the BI + ML approach are shown in Figure 6. Simulated and experimental load-displacement curves match reasonably well. MAPE for median and MAP fitted parameters is 12.2% and 12.1% respectively. The model calibration was performed using axial load and local shear strain data with the specimen in a mixed loading mode. The loading mode in this validation test was axial. Considering that the calibration was performed in the mixed loading mode vs. the validation with uniaxial loading mode, this validation shows that the calibration is robust. The dogbone specimen used in this simple validation study is different compared to the dogbone specimen used in Section 3.1. This dogbone was manufactured from a planar Nitinol strip material, while the dogbone in Section 3.1 was manufactured from a Nitinol tubing material. Nitinol strip and tube materials exhibit different mechanical properties.

4. Discussion

4.1. Propagation of Material Parameter Uncertainty to Simulations of Cyclic Loading

The material parameter uncertainties obtained using the BI + ML calibration approach above can be propagated to any subsequent simulations of

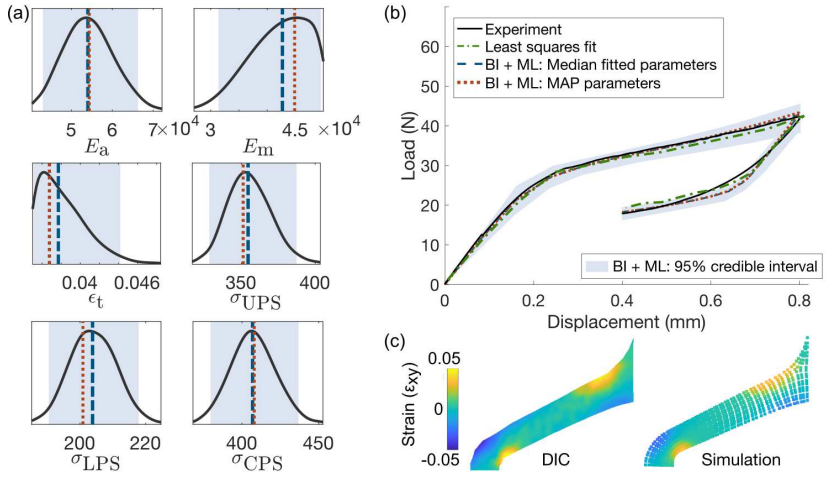


Figure 5: Results of BI + ML calibration with global load and surface strains as the quantity of interest. (a) Marginal posterior probability distributions of the six NiTi material model parameters sampled using the Markov-chain Monte Carlo scheme from a comparison of diamond tensile test, DIC strain field data, and simulations. The simulation library was enriched using a machine learning surrogate model in this case. (b) A qualitative comparison of the calibration on the same diamond geometry. Load-displacement data from the tensile test is shown. (c) Comparison of the local shear strain at peak displacement as measured using DIC and from a simulation with the median fitted material properties.

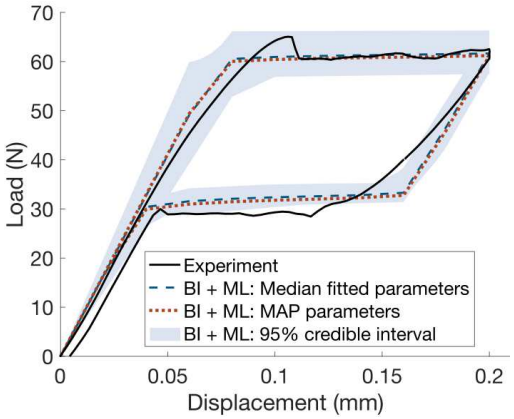


Figure 6: A simple validation of the BI + ML calibrated parameters obtained from the diamond geometry. The validation simulation was performed on a planar dogbone simulation geometry. The experimental data were obtained from tensile test of a planar dogbone specimen fabricated from the identical material as that used to make the diamond samples.

superelastic deformation. We discuss the consequences of propagating the material parameter uncertainties. One of the most common purposes of simulations using the superelastic model is to assess the fatigue performance of a medical device fabricated from NiTi [29]. The simulations designed for this purpose typ-

ically impose a mean displacement and a cyclic displacement amplitude on the component as schematically shown in Figure 7(a). The distribution of the local mean strain and strain amplitude in the device during a fatigue loading cycle is then simulated, resulting in a *point cloud* of the strains as shown in Figure 7(b). The critical mean strain and the critical strain amplitude in the point cloud are typically used as the fatigue indicator parameters for the NiTi device and a fatigue safety factor (FSF) is calculated from them. Any uncertainty in the simulation inputs can naturally introduce an uncertainty in the FSF calculation. To demonstrate the utility of the BI calibration approach presented here, we illustrate how the uncertainty in the superelastic NiTi material parameters can propagate to a simulation of fatigue deformation. We created a simulation of the diamond geometry shown in Figure 2(b) with an imposed mean displacement of 1.0 mm and a displacement amplitude of 0.4 mm. We created 200 instances of this simulation with material parameters sampled within the 95% credible interval for the BI + ML fit described in Section 3.2. We extracted the strain tensor at each integration point in the model at the two extrema of the fatigue loading cycle marked by D and E in Figure 7(a). We calculated the mean strain $\boldsymbol{E}_{\text{mean}}$ and the strain amplitude $\boldsymbol{E}_{\text{amp}}$ at each integration point as,

$$\boldsymbol{E}_{\text{mean}} = \frac{1}{2}\left(\boldsymbol{E}_{\text{D}} + \boldsymbol{E}_{\text{E}}\right),\ \boldsymbol{E}_{\text{amp}} = \frac{1}{2}\left(\boldsymbol{E}_{\text{D}} - \boldsymbol{E}_{\text{E}}\right), \tag{5}$$

where $\boldsymbol{E}_{\text{D}}$ and $\boldsymbol{E}_{\text{E}}$ is the strain tensor at an integration point at D and E respectively. For each simulation, we calculated the maximum principal invariant of the two strain tensors above at each integration point. A sample scatter plot of the strain amplitude plotted against mean strain is shown in Figure 7(b). We determined the critical strain amplitude and the critical mean strain at the point with the largest value of the maximum principal invariant of $\boldsymbol{E}_{\text{amp}}$.

The probability distribution of the critical mean strain from the 200 simulations is shown in Figure 7(c) and the probability distribution of the strain amplitude is shown in Figure 7(d). In both plots, the result obtained from the median calibrated material properties from the BI + ML approach is marked by a dashed line. The mean strain shows a range of approximately 0.01 and the strain amplitude shows a range of approximately 0.007. FSF calculated from this will show a relatively large variation. Thus, we have demonstrated that the uncertainty information furnished by the BI-based calibration approach can be propagated to fatigue simulations of NiTi and it can result in appreciable uncertainty in the fatigue indicator parameters. Similar to strains, if other fatigue indicator parameters for NiTi such as the phase transformation volume amplitude [30] are extracted from the simulations, then those values will be affected by the material parameter uncertainty as well.

We emphasize that this approach provides a quantification of the material parameter uncertainty that may be propagated to any subsequent simulations of fatigue. However, this approach does not quantify the accuracy of the FSF calculated in this subsequent simulation. The accuracy of the FSF will be certainly dependent on the accuracy of the calibrated material parameters. However, it will also be influenced by the ability of the inherent material model in simulating

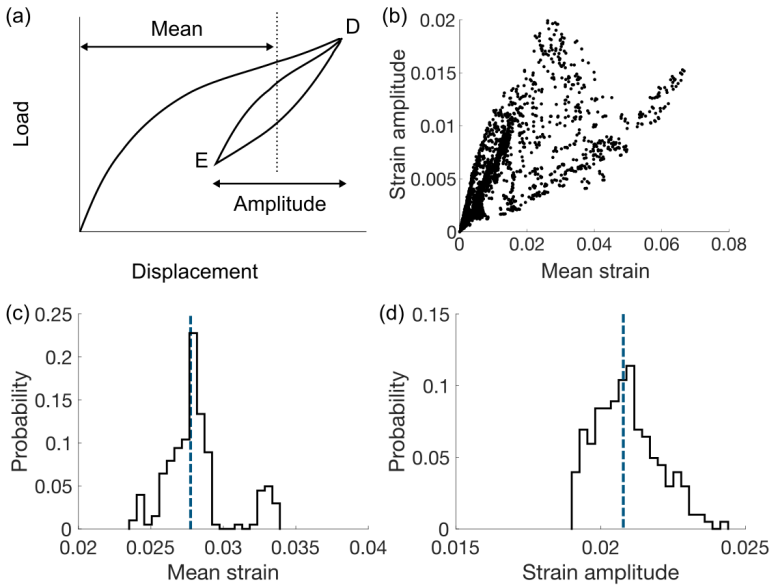


Figure 7: A demonstration of the propagation of material parameter uncertainties to a subsequent simulation. (a) Schematic load-displacement curve of a fatigue-type loading characterized by a mean displacement and a displacement amplitude. (b) A representative scatter plot of the strain amplitude vs. mean strain at finite element model integration points calculated from the loading states D and E shown in (a). (c) Distribution of mean strain and (d) strain amplitude for fatigue loading simulations performed with the material parameter probability distribution obtained using the BI + ML approach.

the fatigue indicator parameters, the accuracy of the underlying finite element model (e.g., geometry and mesh resolution), and any other assumptions made in the simulations.

4.2. Accuracy of Local Compressive Strain Prediction from the Calibrated Parameters

While using the BI approach has benefits over the least-squares calibration approach and using the diamond geometry for calibrating the NiTi superelasticity model has benefits over the use of only simple tension test data, neither the BI approach nor the specimen geometry can overcome the limitations of the underlying constitutive model. In this section we discuss one key example of such limitations. One motivation behind using the full-field surface strain data was to obtain such calibrated material parameters that will furnish a more accurate simulated local strain distribution compared to the calibration with just the global load data. We showed above that the BI + ML approach using strain and load QoI indeed furnished more accurate local strains in terms of the MAPE compared to when a similar calibration was performed using only the load QoI. However, it is worth comparing the BI + ML calibration results with the DIC data in detail. Thus, we compare the simulated local strain distribution

from the optimum calibrated material parameters with the experimental data obtained using DIC. To emphasize, these strains are for the diamond BI + ML calibration results when both strain and load QoI were used.

A comparison of the simulated local shear strains (represented in terms of simulation QoI) with the DIC measurements (represented in terms of experimental QoI) in two key regions of the diamond sample at the peak load is shown in Figure 8. As described in Section 2.3.2, strains averaged over four key regions in the diamond geometry served as the QoIs along with the global load in the demonstration of BI + ML calibration approach. Two of those regions – marked ② and ④ in Figure 2(c) – exhibit compressive strains. In the figure, we have plotted the simulated strains in these two regions as a function of the ratio $\sigma_{\mathrm{CPS}}/\sigma_{\mathrm{UPS}}$. The relative error in the strain prediction from the median or MAP material parameter fit with respect to the experimental measurement is up to 25%. While this is undesirable, it is unavoidable considering that the model consistently underestimated the strains in some regions irrespective of the material parameters used as shown in Figure 8(b). The phenomenological constitutive model considered in this study approximates the NiTi deformation as isotropic, among other assumptions [16]. As a consequence of this, the accuracy of the simulated local compressive strains from the calibrated material properties is modest.

In the same figure, it can be seen that the ratio $\sigma_{\mathrm{CPS}}/\sigma_{\mathrm{UPS}}$ is 1.3 for the median fit and 1.0 for MAP from the BI + ML approach with the 95% credible interval values in between. While the ratio is typically taken as 1.5 for NiTi in tube form, 1.0 to 1.3 is a reasonable number for NiTi strip material. The strip material has a texture with a strong $\langle 1\,1\,0 \rangle$ component [31]. A simple calculation using the crystallographic theory of martensite [32] and mechanics reveals that $\sigma_{\mathrm{CPS}}/\sigma_{\mathrm{UPS}} = 1.0$ for [1 1 0] orientation and the ratio increases for orientations towards [1 1 1], ultimately reaching 1.5 (See Supplementary Data for details of the calculation). Thus, while the local compressive strain predictions with the fitted material parameters are lacking due to the model limitations, the $\sigma_{\mathrm{CPS}}/\sigma_{\mathrm{UPS}}$ ratio is reasonably calibrated. The MAP estimate of 1.0 for this ratio is also consistent with the observations in the literature for [1 1 0] oriented single crystals [22].

4.3. Advantages and Challenges of the BI Calibration Approach

A clear benefit of the BI approach to calibrating constitutive models is the information about uncertainty in the fit obtained from them. This material parameter uncertainty, together with other uncertainties can be propagated to subsequent simulations as we demonstrated. The benefit of using an ML-based surrogate model is that it can improve the parameter fit by enriching the simulation library used in the calculation of likelihood function. The approach presented here is quite general and can be implemented for any model for superelastic deformation. Also, this approach can incorporate essentially any QoI in the calibration process as long as it can be extracted from the simulations built with that constitutive model. In particular, the use of strain QoI resulted in a more accurate simulation of the local strains compared to using only the

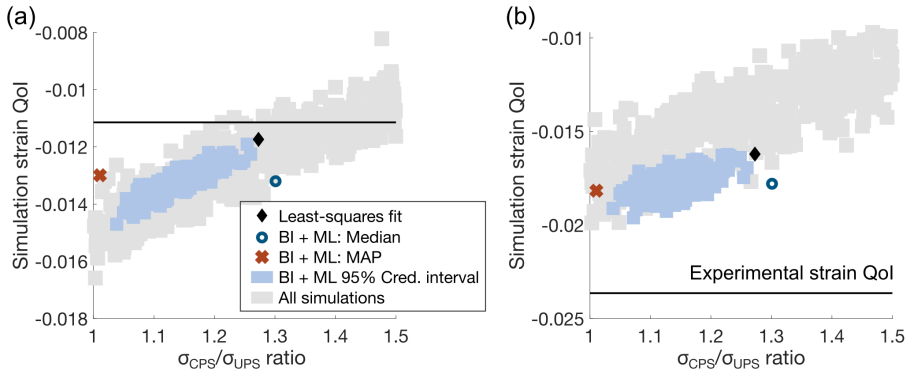


Figure 8: Accuracy of the compressive local strain prediction using the calibrated material properties. (a) Comparison of simulated strain QoI with experimental (DIC) strain QoI in region (2) in Figure 2(c) at peak load shown in Figure 2(b) by point B. (b) Comparison of simulated strain QoI with experimental (DIC) strain QoI in region (4) in Figure 2(c) at peak load. The simulated strains are lower in magnitude than the DIC measurement which is shown by a black horizontal line in both plots. The QoIs are calculated using the shear strain component.

load as the experimental comparator. The diamond geometry furnishes both tensile and compressive response in different regions and allows the calibration of both tensile and compressive model parameters from a single test.

A key challenge associated with this approach compared to the least-square or trial-and-error calibration is the relatively large upfront effort required in setting up the calibration scheme. It requires the construction of a simulation library for a specific test geometry and test method specification. However, once such a library is established, it can be used for any subsequent calibration using the same test setup. An informed choice between this sophisticated calibration method and alternatives can be made by setting concrete expectations about the credibility of simulations for a specific context of use. Frameworks such as the ASME V&V 40 standard can be used for this purpose [33]. For example, if the model risk is high for a particular context of use, then investing in the BI calibration scheme could be desirable to ensure the influence of material parameters and their uncertainty is rigorously considered. However, if the model risk is low, then a simpler calibration approach may be used to obtain the nominal material properties.

Implementation and execution of this calibration method requires certain subjective inputs on the part of the analyst. For example, prior distribution of the material parameters is a subjective choice. We demonstrated that the calibrated material parameters from the posterior distribution can be estimated using point estimates such as median and MAP. However, it is a subjective choice to select a particular point estimate. The weights used in calculating the likelihood function are also a subjective choice. However, these subjective choices present an opportunity to incorporate the specialist's knowledge about the constitutive response in the calibration scheme.

Since the likelihood function is calculated from a comparison of the simulated and the experimentally observed response of the QoIs, the accuracy of calibration may be impacted by the limitations of the test setup and the limitations of the underlying model itself. For example, an incorrect DIC setup can furnish an inaccurate surface strain distribution, which will impact the calibration. In Section 4.2 we reported the modest accuracy of the local strains simulated using the calibrated parameters due to the limitations of the model itself. We also attempted to use the full strain tensor in four regions (①-④ in Figure 2(c)) as the QoI in the diamond calibration example. However, the results were not superior to the case when the shear strain component was used as the quantity of interest. We found that the finite element model used in this study was able to capture the shear strains more accurately compared to the normal strain components (See supplementary Data for additional details). Additionally, the SVM surrogate model accuracy was lower for the normal strain components. These factors plausibly lead to the strain tensor-based calibration approach not yielding superior results to the approach using only the shear strain component. Thus, ensuring that the test methods furnish robust data, appropriate QoIs are selected to perform the calibration, and the underlying forward model is accurate are the responsibilities of the specialist to ensure that reliable calibrated material parameters are obtained and the simulation results from such parameters are accurate.

There are several opportunities to further refine this calibration approach and the communication of calibration results. There is significant prior work on incorporating individual sources of uncertainty in the Bayesian calibration procedure [5, 34]. This work can be extended to individually assess the impact of various sources of uncertainty on the calibrated parameters. We extensively documented the effect of model error on the accuracy of calibration. Various efforts have suggested methods to account for and reduce the impact of model error or uncertainty on the calibration procedure [4, 35]. We presented the uncertainty in the calibrated material parameters in terms of the credibility interval. The credibility intervals may be reported in various ways including the highest posterior density interval (HPI) or equal-tailed interval [8]. One of such representations that is the most informative may be chosen when reporting the uncertainty.

5. Summary and Conclusions

We presented the implementation of a Bayesian Inference material property calibration approach for a constitutive model to simulate the superelastic deformation of NiTi shape memory alloy. We made three contributions as part of this approach:

1. We presented a diamond standard specimen geometry that can be used to calibrate both tensile and compressive material parameters. This is significant considering that the constitutive response of NiTi is asymmetric in tension vs. compression.

2. We demonstrated a method to incorporate full-field surface strain data obtained using digital image correlation in the calibration process. This is significant because full-field strain data furnishes a large number of comparators in the calibration process and can contribute to increasing the accuracy of the calibration. Incorporation of surface strain data also resulted in model parameters that furnish more accurate local strain distributions and a more accurate determination of the fatigue safety factor from the simulations.
3. We demonstrated that a relatively simple machine learning surrogate model can be used to enrich the simulation library used in the calibration. This is significant because generating a simulation library using a nonlinear constitutive law such as that used in this work is challenging. The surrogate model can enable performing high-quality calibration in a computationally efficient manner.

The key advantage of the Bayesian Inference approach is that it furnishes uncertainty in the calibrated material parameters and that uncertainty can be propagated to subsequent simulations. While we applied the calibration scheme to the Auricchio and Taylor [16] model for superelastic response implemented in Abaqus finite element modeling framework, this method is versatile and can be applied to other models for the deformation of NiTi SMA. The ultimate accuracy of simulations conducted with the calibrated material parameters, however, depends on the ability of the underlying constitutive model to accurately capture the physics of the material response.

6. Data Availability

The raw data required to reproduce these findings cannot be shared at this time due to technical or time limitations. The processed data required to reproduce these findings are available to download from `https://github.com/confluentmedical/nitinol-bayes-cal`. Annotated computer code to perform this calibration is available at `https://github.com/confluentmedical/nitinol-bayes-cal`.

7. CRediT Author Statement

Harshad M. Paranjape: Conceptualization, Methodology, Software, Formal analysis, Investigation, Writing - Original draft. Kenneth I. Aycock: Methodology, Writing - Original draft. Jason D. Weaver, Brent A. Craven: Methodology. Craig Bonsignore, Thomas W. Duerig: Resources. All authors: Writing - Review & Editing.

8. Acknowledgement

HMP would like to thank Confluent Medical Technologies, Inc. for testing and computational resources. The findings and conclusions in this article have

not been formally disseminated by the U.S. FDA and should not be construed to represent any agency determination or policy. The mention of commercial products, their sources, or their use in connection with material reported herein is not to be construed as either an actual or implied endorsement of such products by the Department of Health and Human Services.

9. References

[1] E. van der Giessen, P. A. Schultz, N. Bertin, V. V. Bulatov, W. Cai, G. Csányi, S. M. Foiles, M. G. D. Geers, C. González, M. Hütter, W. K. Kim, D. M. Kochmann, J. LLorca, A. E. Mattsson, J. Rottler, A. Shluger, R. B. Sills, I. Steinbach, A. Strachan, E. B. Tadmor, Modelling Simul. Mater. Sci. Eng. 28 (2020) 043001. doi:10.1088/1361-651X/ab7150.

[2] T. M. Morrison, P. Pathmanathan, M. Adwan, E. Margerrison, Front Med (Lausanne) 5 (2018). doi:10.3389/fmed.2018.00241.

[3] X. Liu, United States, National Aeronautics and Space Administration, Vision 2040: a roadmap for integrated, multiscale modeling and simulation of materials and systems, 2018. OCLC: 1035419188.

[4] H. Rappel, L. A. A. Beex, J. S. Hale, L. Noels, S. P. A. Bordas, Arch Computat Methods Eng 27 (2020) 361–385. doi:10.1007/s11831-018-09311-x.

[5] C. Gogu, R. Haftka, R. Le Riche, J. Molimard, A. Vautrin, AIAA Journal 48 (2010) 893–903. doi:10.2514/1.40922.

[6] P. Liu, S.-K. Au, Probabilistic Engineering Mechanics 34 (2013) 101–109. doi:10.1016/j.probengmech.2013.08.005.

[7] A. Castillo, S. R. Kalidindi, Front. Mater. 6 (2019). doi:10.3389/fmats.2019.00136, publisher: Frontiers.

[8] D. E. Ricciardi, O. A. Chkrebtii, S. R. Niezgoda, Integr Mater Manuf Innov 8 (2019) 273–293. doi:10.1007/s40192-019-00154-3.

[9] J. H. Crews, R. C. Smith, in: Behavior and Mechanics of Multifunctional Materials and Composites 2012, volume 8342, International Society for Optics and Photonics, 2012, p. 83421N. doi:10.1117/12.914792.

[10] P. Honarmandi, T. C. Duong, S. F. Ghoreishi, D. Allaire, R. Arroyave, Acta Materialia 164 (2019) 636–647. doi:10.1016/j.actamat.2018.11.007.

[11] S. Avril, M. Bonnet, A.-S. Bretelle, M. Grédiac, F. Hild, P. Ienny, F. Latourte, D. Lemosse, S. Pagano, E. Pagnacco, F. Pierron, Exp Mech 48 (2008) 381. doi:10.1007/s11340-008-9148-y.

[12] J. Réthoré, Int. J. Numer. Meth. Engng. 84 (2010) 631–660. doi:10.1002/nme.2908.

[13] M. Bertin, C. Du, J. P. Hoefnagels, F. Hild, Acta Materialia 116 (2016) 321–331. doi:10.1016/j.actamat.2016.06.039.

[14] L. Wu, K. Zulueta, Z. Major, A. Arriaga, L. Noels, Computer Methods in Applied Mechanics and Engineering 360 (2020) 112693. doi:10.1016/j.cma.2019.112693.

[15] L. Lu, M. Dao, P. Kumar, U. Ramamurty, G. E. Karniadakis, S. Suresh, PNAS 117 (2020) 7052–7062. doi:10.1073/pnas.1922210117, publisher: National Academy of Sciences Section: Physical Sciences.

[16] F. Auricchio, R. Taylor, J. Lubliner, Computer Methods in Applied Mechanics and Engineering 146 (1997).

[17] K. P. Murphy, Machine learning: a probabilistic perspective, Adaptive computation and machine learning series, MIT Press, Cambridge, MA, 2012.

[18] A. Vigliotti, G. Csányi, V. S. Deshpande, Journal of the Mechanics and Physics of Solids 118 (2018) 74–97. doi:10.1016/j.jmps.2018.05.007.

[19] I. Babuška, Z. Sawlan, M. Scavino, B. Szabó, R. Tempone, Computer Methods in Applied Mechanics and Engineering 304 (2016) 171–196. doi:10.1016/j.cma.2016.02.013.

[20] V. Vapnik, Statistical learning theory, Adaptive and learning systems for signal processing, communications, and control, Wiley, 1998.

[21] F. Auricchio, R. Taylor, Computer Methods in Applied Mechanics and Engineering 143 (1997).

[22] K. Gall, H. Sehitoglu, Y. Chumlyakov, I. Kireeva, Acta Materialia 47 (1999) 1203–1217. doi:10.1016/S1359-6454(98)00432-7.

[23] K. Gall, International Journal of Plasticity 15 (1999) 69–92. doi:10.1016/S0749-6419(98)00060-6.

[24] F04 Committee, Test Method for Tension Testing of Nickel-Titanium Superelastic Materials, Technical Report, ASTM International, ???? URL: http://www.astm.org/cgi-bin/resolver.cgi?F2516-18. doi:10.1520/F2516-18.

[25] A. Grinsted, Ensemble MCMC sampler, 2020. URL: https://www.github.com/grinsted/gwmcmc.

[26] K. I. Aycock, J. D. Weaver, H. M. Paranjape, K. Senthilnathan, C. Bonsignore, B. A. Craven, Journal of the Mechanical Behavior of Biomedical Materials (In review). doi:10.31224/osf.io/a3twm.

[27] J. Blaber, B. Adair, A. Antoniou, Experimental Mechanics 55 (2015) 1105–1122. doi:10.1007/s11340-015-0009-1.

[28] T. W. Duerig, K. Bhattacharya, Shape Memory and Superelasticity 1 (2015) 153–161. doi:10.1007/s40830-015-0013-4.

[29] A. R. Pelton, X.-Y. Gong, T. Duerig, Proceedings of SMST 2003 (2003) 9.

[30] H. M. Paranjape, B. Ng, I. Ong, L. Vien, C. Huntley, Scripta Materialia 178 (2020) 442–446. doi:10.1016/j.scriptamat.2019.12.014.

[31] S. W. Robertson, V. Imbeni, H.-R. Wenk, R. O. Ritchie, J. Biomed. Mater. Res. 72A (2005) 190–199. doi:10.1002/jbm.a.30214.

[32] K. Bhattacharya, Microstructure of Martensite: Why It Forms and How It Gives Rise to the Shape-Memory Effect, Oxford Series on Materials Modelling, Oxford University Press, Oxford, New York, 2004.

[33] ASME, Assessing Credibility of Computational Modeling Through Verification and Validation: Application to Medical Devices, Technical Report, 2018.

[34] M. C. Kennedy, A. O'Hagan, J Royal Statistical Soc B 63 (2001) 425–464. doi:10.1111/1467-9868.00294.

[35] C. Jiang, Z. Hu, Y. Liu, Z. P. Mourelatos, D. Gorsich, P. Jayakumar, Computer Methods in Applied Mechanics and Engineering 368 (2020) 113172. doi:10.1016/j.cma.2020.113172.

A Probabilistic Approach with Built-in Uncertainty Quantification for the Calibration of a Superelastic Constitutive Model from Full-field Strain Data: Supplementary Material

Harshad M. Paranjape[a,*], Kenneth I. Aycock[b], Craig Bonsignore[a], Jason D. Weaver[b], Brent A. Craven[b], Thomas W. Duerig[a]

[a] *Confluent Medical Technologies, Inc. 47533 Westinghouse Drive, Fremont, CA 94539, United States.*
[b] *U.S. Food and Drug Administration, Center for Devices and Radiological Health, Office of Science and Engineering Laboratories, Division of Applied Mechanics., Silver Spring, MD 20993, United States.*

1. Quantities of Interest and Weights

For the demonstration of Bayesian Inference (BI) approach for material parameter calibration using the dogbone specimen in Section 2.3.1, the quantities of interest (QoI) are the global stress values at 82 points along the stress-strain curve. The stress data is extracted at points equidistant in time and since the test is performed at constant strain rate, the points are equally separated in strain. The weights used in the objective function calculation for the least-squares fitting and for the calculation of the likelihood function were taken proportional to the local slope of the load-displacement data for the corresponding experiment. The motivation behind such a choice is that this gave relatively equal weight to the elastic regime and the plateau or the transformation regime during fitting. Without the weights, the transformation plateau data was overfitted and the elastic regime data was underfitted because there were relatively few data points in the elastic regime. The weight w_i used in Equation 1 are listed below:

$$\begin{aligned}\boldsymbol{w} = [&0.00, 29.78, 103.5, 115.6, 86.7, 0.32, 1.54, 2.24,\\ &2.13, 1.88, 2.63, 2.25, 2.53, 2.25, 2.75, 2.49,\\ &2.99, 3.08, 2.93, 3.51, 3.54, 70.0, 91.1, 61.4,\\ &47.9, 29.9, 14.9, 4.96, 4.23, 2.79, 2.79, 2.02,\\ &2.00, 0.95, 2.02, 2.22, 2.22, 2.70, 4.00, 7.39,\\ &12.8, 0.00, 34.5, 86.5, 93.5, 79.1, 29.4, 3.92,\\ &1.63, 1.56, 1.06, 2.32, 1.68, 1.74, 1.48, 2.29,\\ &2.01, 1.86, 1.71, 2.52, 2.14, 2.72, 2.74, 3.82,\\ &3.02, 3.07, 2.68, 37.66, 44.7, 49.6, 60.4, 66.8,\\ &63.7, 66.9, 64.1, 63.1, 56.5, 52.2, 47.6, 39.5,\\ &37.1, 31.4].\end{aligned} \tag{S1}$$

For the demonstration of BI and machine learning (ML) approach in 2.3.2, a total of 110 QoIs are used. The QoIs correspond to 1 global load and 4 averaged local strain values measured at 22 frames in the experiment and in the simulation. In this case, the weights were chosen such that the data points near the

*Corresponding author
Email address: harshad.paranjape@confluentmedical.com (Harshad M. Paranjape)

maximum load received a larger weight compared to the data points near the origin of the load-displacement data. Also, the strain and load QoIs received equal weight overall. The weights used in Equation 1 for this case are as follows:

$$\begin{aligned}\boldsymbol{w} = [&0.00, 0.00, 0.00, 0.00, 0.01, 0.00, 0.00, 0.00,\\ &0.00, 0.01, 0.03, 0.03, 0.03, 0.03, 0.10, 0.03,\\ &0.03, 0.03, 0.03, 0.10, 0.30, 0.30, 0.30, 0.30,\\ &1.20, 0.35, 0.35, 0.35, 0.35, 1.40, 0.35, 0.35,\\ &0.35, 0.35, 1.40, 0.35, 0.35, 0.35, 0.35, 1.40,\\ &0.40, 0.40, 0.40, 0.40, 1.60, 0.40, 0.40, 0.40,\\ &0.40, 1.60, 0.50, 0.50, 0.50, 0.50, 2.00, 0.50,\\ &0.50, 0.50, 0.50, 2.00, 0.50, 0.50, 0.50, 0.50,\\ &2.00, 0.50, 0.50, 0.50, 0.50, 2.00, 0.50, 0.50,\\ &0.50, 0.50, 2.00, 0.50, 0.50, 0.50, 0.50, 2.00,\\ &0.50, 0.50, 0.50, 0.50, 2.00, 0.50, 0.50, 0.50,\\ &0.50, 2.00, 0.50, 0.50, 0.50, 0.50, 2.00, 0.50,\\ &0.50, 0.50, 0.50, 2.00, 0.50, 0.50, 0.50, 0.50,\\ &2.00, 0.38, 0.38, 0.38, 0.38, 1.50].\end{aligned} \tag{S2}$$

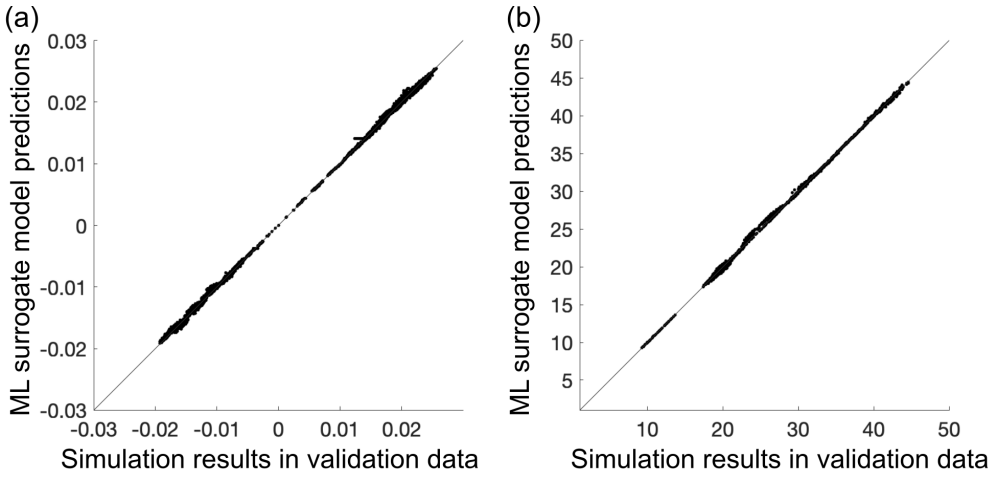


Figure S1: Verification of machine learning surrogate model. In the machine learning terminology, this is often referred to as *model validation*. (a) Strain QoI prediction from the fitted surrogate model compared with the output of the full simulation. (b) Load QoI from the surrogate model compared to the simulation results.

2. Machine Learning Model Verification

The development of a surrogate model for predicting QoIs from arbitrary material parameters is described in Section 2.2. The surrogate model is developed using kernel support vector machine (SVM), which is a machine learning (ML) regression scheme. It is customary to verify a regression model by making predictions on inputs which were not used in training the model. We use the term *verification* in this work in the sense of *Verification, validation, and uncertainty quantification* VVUQ methodology [1]. In ML terminology, this is often referred to as *model validation*. While cross-validation is one popular method of doing this, we chose to run separate simulations using a set of material parameters and then validated the model on these separate simulations. We ran 200 simulations with the diamond geometry identical to those described in Section

2.3.2. These simulations used a range of material parameters uniformly sampled from the 95% credible interval of the results described in Section 2.3.2. Then, we used the SVM regression model that was trained on the library of 544 simulations and used it to predict the QoIs in 100 of these simulations. A comparison of the QoIs obtained from the simulations and those predicted by the fitted model is shown in Figure S1. Separate plots are shown for the strain QoI and load QoI since their values are of different magnitudes. The fitted regression model made excellent predictions for these data with $R^2 = 0.99993$. Based on this verification study, the SVM regression model appears to be accurate.

3. Effect of Prior on the Results

In BI, the choice of prior distribution can influence the predicted posterior distribution [2]. While a rigorous study of the influence of prior on the results is not within the scope of this work, we performed a limited study to understand the effect of prior distribution on the calibrated material parameters. We considered four types of prior distributions for the material parameters: one flat prior and three Gaussian priors with varying mean and standard deviation. Starting with these priors, we determined the posterior distributions using the same procedure described in Section 2.3.2. The results of this comparison are shown in Figure S2. From the results, it is evident that the choice of prior did not have a significant impact on the predicted posterior distribution in this material parameter calibration study.

4. Theoretical Calculation of Compression-Tension Plateau Ratio

The ratio of compression plateau stress to tension plateau stress in superelastic NiTi can be theoretically approximated as a function of crystal orientation or texture using simple concepts from micromechanics and crystallography. The plateau stresses are connected to the A $\leftrightarrow$ M phase transformation induced by an external stress. It is customary to model the phase transformation using a transformation condition. Following Anand and Gurtin [3], a simple transformation condition can be written as,

$$Y^i = \boldsymbol{b}_0^i \cdot (\boldsymbol{C}^{\mathrm{e}}\boldsymbol{T}^{\mathrm{e}})\boldsymbol{m}_0^i - \frac{\lambda_{\mathrm{T}}}{\theta_{\mathrm{T}}}(\theta - \theta_{\mathrm{T}}) - \sum_{j=1}^{N} h^{ij}\nu^j \text{ for A} \rightarrow \text{M}. \tag{S3}$$

Here Y^i is the critical driving force for activating i^{th} habit plane variant (hpv) system, $\boldsymbol{b}_0^i$ and $\boldsymbol{m}_0^i$ are the shear direction and normal for the i^{th} hpv in the global coordinate system, $\boldsymbol{C}^{\mathrm{e}}$ is the elastic right Cauchy-Green tensor, $\boldsymbol{T}^{\mathrm{e}}$ is the work conjugate to the Cauchy-Green elastic strain, λ_{T} is the latent heat per unit volume for the A $\rightarrow$ M phase transformation, θ is the reference temperature, θ_{T} is the equilibrium transformation temperature, h^{ij} is a transformation hardening parameter, ν^i is the volume fraction of the i^{th} hpv system, and N is the total number of hpvs modeled. The hpv elements $(\boldsymbol{b}_0^i, \boldsymbol{m}_0^i)$ are material parameters and can be derived using the crystallographic theory of martensite (CTM) [4] if the lattice parameters for austenite and martensite phases are known. CTM typically furnishes these parameters in the crystal coordinates $(\boldsymbol{b}_{\mathrm{c}}^i, \boldsymbol{m}_{\mathrm{c}}^i)$ and the transformation in the crystal and global coordinate systems can be performed using: $\boldsymbol{b}_0^i = \boldsymbol{G}\boldsymbol{b}_{\mathrm{c}}^i, \boldsymbol{m}_0^i = \boldsymbol{G}\boldsymbol{m}_{\mathrm{c}}^i$. Here $\boldsymbol{G}$ is the orientation tensor. Assuming the case of infinitesimal deformation, absence of transformation hardening, isothermal conditions, and uniaxial loading, all terms in the equation above except the first term are constant and the transformation condition can be approximated in the following form,

$$\boldsymbol{S}_0^i \cdot \boldsymbol{\sigma} = k. \tag{S4}$$

Here $\boldsymbol{S}_0^i = \boldsymbol{b}_0^i \otimes \boldsymbol{m}_0^i$ is the Schmid tensor for the i^{th} hpv system and k is a constant. Moreover, k does not depend whether loading is performed in tension vs. compression. At the onset of stress-induced A $\rightarrow$ M phase transformation, it is reasonable to assume that the hpv with the largest component along the direction of stress is activated. If the Schmid factor for this hpv system is defined as S_0^{T} for tensile loading and S_0^{C}

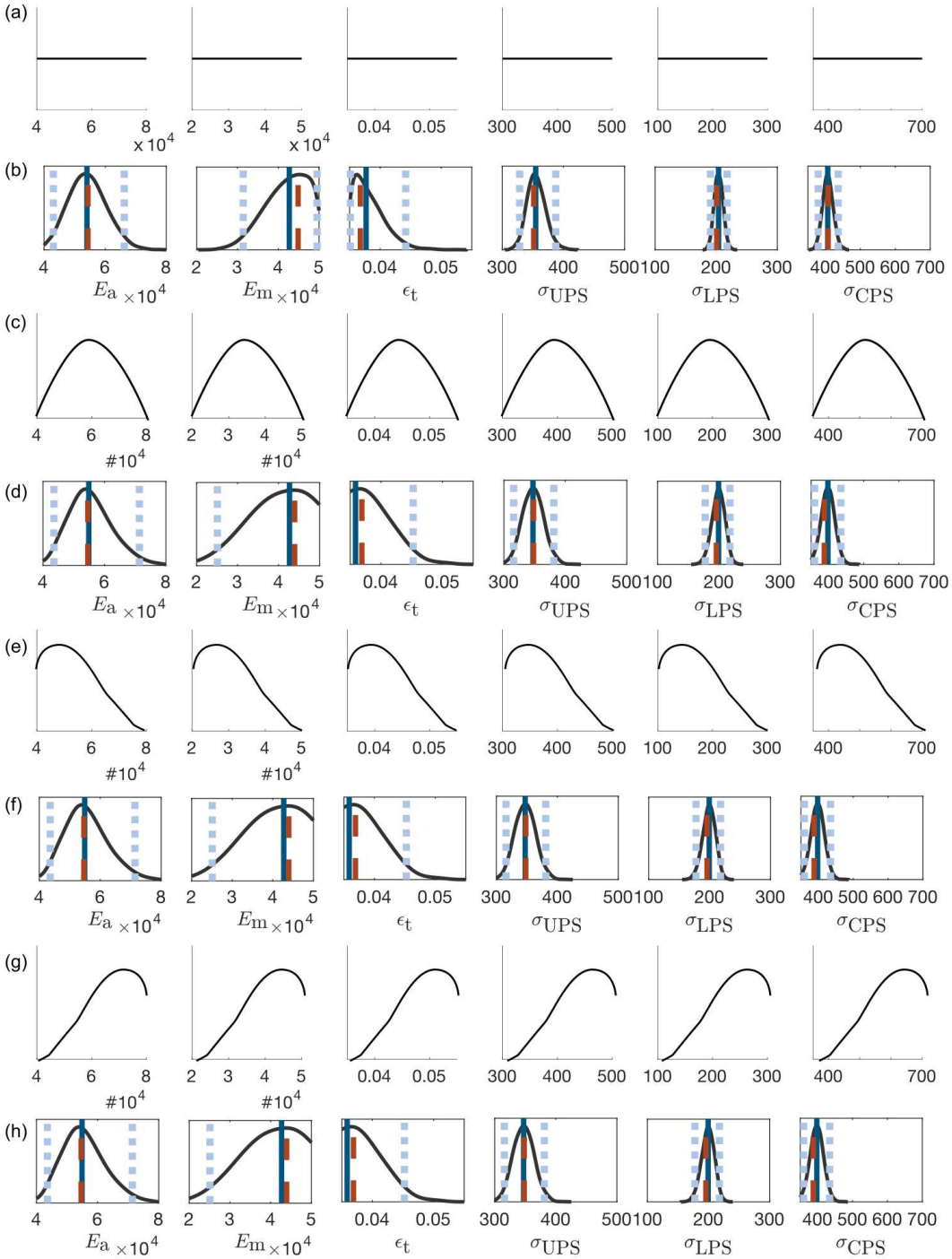


Figure S2: Effect of prior distribution on the sampled posterior probability distribution from the Markov Chain Monte Carlo process. (a, c, e, g) Four prior distributions. (a) shows a flat prior and (c, e, g) show Gaussian priors with various mean and standard deviation. (b, d, f, h) The sampled marginal posterior distributions. The prior does not significantly influence the posterior.

for compressive loading, then we can write, $S_0^{\mathrm{T}}\sigma_{\mathrm{UPS}} = S_0^{\mathrm{C}}\sigma_{\mathrm{CPS}} = k$. Thus, the ratio of plateau stress in

compression and the plateau stress in tension can be written as,

$$\frac{\sigma_{\text{CPS}}}{\sigma_{\text{UPS}}} = \frac{S_0^{\text{T}}}{S_0^{\text{C}}}. \tag{S5}$$

This calculation can be performed for any crystal orientation. The computer code for the calculation of S is publicly available [5]. The ratio $\sigma_{\text{CPS}}/\sigma_{\text{UPS}}$ for NiTi using typical lattice parameters is plotted on the inverse pole figure in Figure S3. The rolling texture of a NiTi tube has a large [1 1 1] directional component along the drawing direction. The calculated $\sigma_{\text{CPS}}/\sigma_{\text{UPS}}$ ratio for tube is thus close to 1.5. For a plate or sheet, the texture along rolling direction has a large [1 1 0] component. The calculated ratio for this case is close to 1.0.

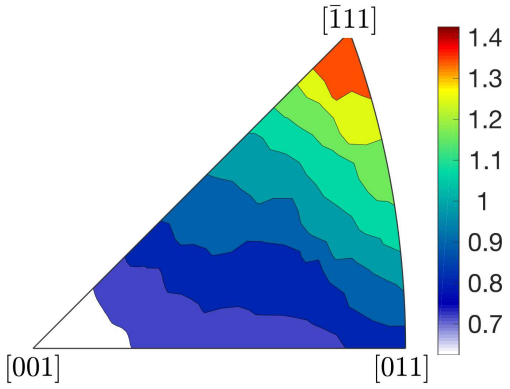


Figure S3: The ratio of compression plateau stress to tension plateau stress based on crystallographic calculations.

5. Experiment-Simulation Comparison of All Strain Components

The calibration scheme presented in this work used the shear strain component (ε_{xy}) as a QoI. We also attempted to perform the calibration using the full 2D surface strain tensor as the QoI. However, the latter approach did not furnish more accurate results compared to shear strains. We primarily attribute this to the inability of the finite element model used in this study to capture the normal strain components. A comparison of all simulated strain components and experimentally measured strain components (using DIC) in regions of interest ① to ④ as a function of the loading step is shown in Figure S4. These data are for the diamond specimen discussed in Section 3.2. We calculated a least-squared fit for the six material parameters using the approach described in Section 2, Equation 1. We calculated mean absolute percentage error (MAPE) between the DIC measurement and the least-square fit for each strain component in each region of interest of the diamond sample (See Figure 2(c)). The total MAPE for ε_{xx} strain components summed over the four regions of interest was 152.5. MAPE for ε_{yy} summed over the four regions of interest was 462.7, and MAPE for ε_{xy} strain component was 105.3 when summed over the same four regions of interest. This shows that the underlying constitutive law was able to capture the shear strains more accurately compared to the normal strains. Based on this observation, it appears plausible that the calibration using the full strain tensor did not furnish more accurate results compared to the calibration using just the shear strain component.

6. References

[1] ASME, Assessing Credibility of Computational Modeling Through Verification and Validation: Application to Medical Devices, Technical Report, 2018.

[2] H. Rappel, L. A. A. Beex, J. S. Hale, L. Noels, S. P. A. Bordas, Arch Computat Methods Eng 27 (2020) 361–385. doi:10.1007/s11831-018-09311-x.

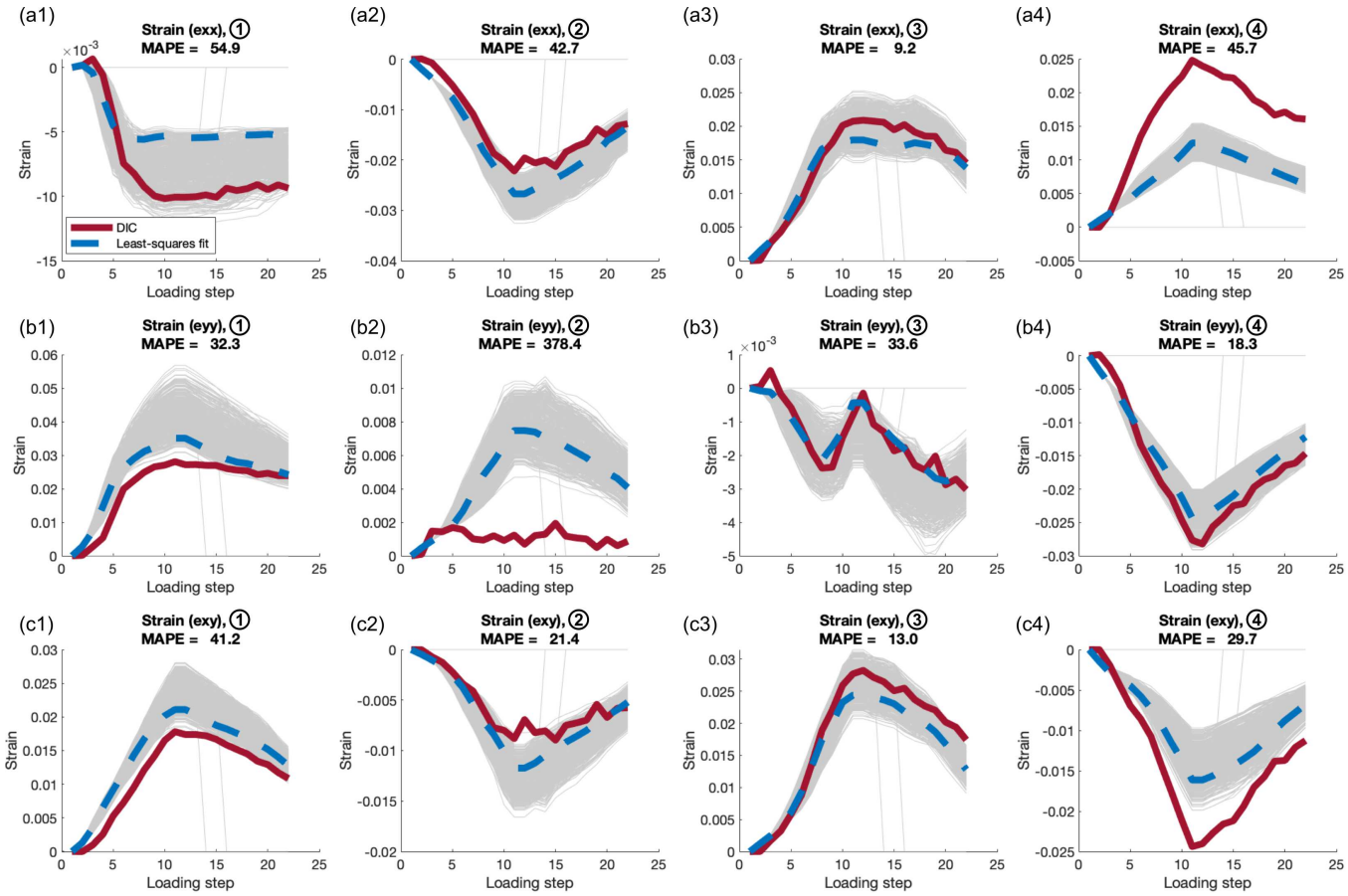


Figure S4: Comparison of the simulated strain components and the DIC strain measurement of the individual strain components for the diamond sample described in Section 3.2. (a1-a4) Normal strain (ε_{xx}) in regions of interest ①-④. (b1-b4) Normal strain (ε_{yy}) in regions of interest ①-④. (c1-c4) Shear strain (ε_{xy}) in regions of interest ①-④. In all cases, the X axis is the loading step. Data was extracted at twenty two points along the tensile loading curve for the diamond sample. The gray curves correspond to all simulations in the library. The red curve corresponds to the DIC strain measurement. The dashed blue curve corresponds to the calibrated parameters using a least-squared approach. MAPE values for the DIC and least-squared fit are listed in each plot. Overall, the shear strains show lower MAPE values.

[3] L. Anand, M. E. Gurtin, Journal of the Mechanics and Physics of Solids 51 (2003) 1015–1058. doi:10.1016/S0022-5096(03)00017-6.

[4] K. Bhattacharya, Microstructure of Martensite: Why It Forms and How It Gives Rise to the Shape-Memory Effect, Oxford Series on Materials Modelling, Oxford University Press, Oxford, New York, 2004.

[5] H. Paranjape, MechanicsNext: Mechanics of Materials Using Numerical and Experimental Techniques, 2017. URL: https://github.com/MechanicsNext/MechanicsNext. doi:10.5281/zenodo.822831, publication Title: GitHub repository.